Environmental Science and Ecotechnology 29 (2026) 100657

Contents lists available at ScienceDirect

Environmental Science and Ecotechnology

journal homepage: www.journals.elsevier.com/environmental-science-and-ecotechnology/

Original Research

Nanoplastics amplify 6PPD ocular toxicity in zebrafish

Jian Lin [a,b,1], Dongliang Pan [a,b,1], Xingxing Chen [c,1], Minyan Xu [b], Yangfan Zhu [b], Yi Zheng [a,b], Yang Song [d,*], Jiangfei Chen [a,b,e,**]

[a] The Second Affiliated Hospital of Wenzhou Medical University, Wenzhou Municipal Key Laboratory of Neurodevelopmental Pathology and Physiology, Wenzhou, 325035, China
[b] School of Public Health, Wenzhou Medical University, Wenzhou, 325035, China
[c] Zhejiang Mariculture Research Institute, Zhejiang Key Laboratory of Coastal Biological Germplasm Resources Conservation and Utilization, Wenzhou, 325000, China
[d] State Key Laboratory of Environmental Chemistry and Ecotoxicology, Research Center for Eco-Environmental Sciences, Chinese Academy of Sciences, Beijing, 100085, China
[e] South Zhejiang Institute of Radiation Medicine and Nuclear Technology, Wenzhou, 325035, China

ARTICLE INFO

Article history:
Received 9 May 2025
Received in revised form
1 January 2026
Accepted 4 January 2026

Keywords:
Zebrafish
Nanoplastics
6PPD
Co-exposure
Ocular toxicity

ABSTRACT

Nanoplastics and tire-derived chemicals are ubiquitous co-pollutants in aquatic environments, originating from road runoff and posing potential risks to vertebrate development through enhanced bioavailability and synergistic toxicity. Polystyrene nanoplastics (PS) can adsorb hydrophobic organics like the antioxidant N-(1,3-dimethylbutyl)-N'-phenyl-p-phenylenediamine (6PPD), acting as vectors that increase tissue accumulation and exacerbate oxidative stress, while 6PPD alone disrupts mitochondrial function and induces sublethal effects in exposed organisms. The vertebrate eye, with its direct environmental exposure and sensitive neural structures, is particularly vulnerable, yet the combined impact of PS and 6PPD on visual morphogenesis remains underexplored. Here we show that co-exposure to environmentally relevant concentrations of PS (1 mg L^{-1}) and 6PPD (0.1–0.8 mg L^{-1}) markedly potentiates ocular toxicity compared to individual exposures, manifesting as myopia-like malformations, increased cell death, and impaired phototaxis. We integrated phenotypic, histological, and multi-omics analyses using zebrafish embryos as a model. Our results show PS-enhanced bioaccumulation of 6PPD in ocular tissues, leading to severe lens and retinal damage, aberrant vascularization, disrupted myelination, and dysregulated pathways including serine proteolysis, retinoic acid metabolism, and ferroptosis-linked oxidative stress. These findings demonstrate nanoplastic-chemical interactions as an emerging threat to aquatic visual function, with implications for survival behaviors and broader ecosystem health under pervasive pollution.

1. Introduction

The exponential rise in plastic production, coupled with inadequate waste management, has established micro- and nanoplastics (MNPs) as pervasive global contaminants [1]. Approximately one-third of total MNPs emissions originate from tire wear particles, which serve as carriers for a complex cocktail of chemical additives [2,3]. Among these, the tire-derived aromatic amine antioxidant N-(1,3-dimethylbutyl)-N'-phenyl-p-phenylenediamine (6PPD) is a ubiquitous antioxidant essential for preventing tire degradation. Consequently, urban runoff and aquatic sinks have become "hotspots" for the co-occurrence of MNPs and 6PPD with environmental concentrations frequently reaching mg L^{-1} levels for MNPs and μg L^{-1} levels for 6PPD [4,5]. Despite their simultaneous presence in dust, soil, and biological fluids [5–7], the ecological risks posed by the combined exposure to these co-pollutants remain poorly understood.

* Corresponding author. State Key Laboratory of Environmental Chemistry and Ecotoxicology, Research Center for Eco-Environmental Sciences, Chinese Academy of Sciences, Beijing, 100085, China.
** Corresponding author. The Second Affiliated Hospital of Wenzhou Medical University, Wenzhou Municipal Key Laboratory of Neurodevelopmental Pathology and Physiology, Wenzhou, 325035, China.
E-mail addresses: yangsong@rcees.ac.cn (Y. Song), feichen@wmu.edu.cn (J. Chen).
[1] Equally contribute to this work.

https://doi.org/10.1016/j.ese.2026.100657

The interaction between MNPs and hydrophobic organic contaminants represents a critical toxicological concern. MNPs undergo environmental weathering that reduces their particle size, increasing their specific surface area and capacity to adsorb co-contaminants—a phenomenon known as the "Trojan Horse" effect [8–10]. This vector potential can significantly alter the bioavailability and body burden of adsorbed chemicals, potentially potentiating their toxicity. While the acute lethality of the 6PPD metabolite, 6PPD-quinone, has been established in salmonids [11], the sublethal developmental toxicity of the parent compound 6PPD, particularly when complexed with nanoplastics, requires urgent investigation. Recent evidence suggests that 6PPD induces oxidative stress and mitochondrial dysfunction [12], while MNPs alone can penetrate biological barriers and accumulate in sensitive tissues [13,14].

The vertebrate visual system is particularly vulnerable to these environmental stressors. Eyes are directly exposed to waterborne and airborne particulates, and MNPs have been shown to penetrate the blood-retina barrier, accumulating in ocular tissues and inducing inflammation [13,15]. Similarly, tire rubber additives have been implicated in ocular injury and vascular mispatterning [16,17]. However, the synergistic impact of MNPs and 6PPD co-exposure on visual development remains a significant knowledge gap. We hypothesize that nanoplastics may act as vectors to enhance the ocular accumulation of 6PPD, leading to compounded visual toxicity through oxidative and apoptotic pathways.

In this study, we utilized zebrafish (*Danio rerio*) as a model vertebrate to evaluate the combined toxicity of polystyrene nanoplastics (PS, 80 nm) and 6PPD. Zebrafish were selected due to the high homology of their visual system with humans and their rapid ocular development [18,19]. PS was chosen as a representative polymer due to its environmental persistence and high adsorption capacity [20]. We employed an integrated approach combining phenotypic analysis, behavioral assays, and dual-omics profiling (transcriptomics and proteomics) to elucidate the molecular mechanisms driving combined ocular toxicity. By using environmentally relevant concentrations of PS (1 mg L^{-1}) [15] and varying levels of 6PPD (0.1–0.8 mg L^{-1}) [21], this study aims to reveal the potential synergistic risks these ubiquitous road-runoff pollutants pose to aquatic visual health.

2. Materials and methods

2.1. Zebrafish husbandry

The present study utilized wild-type AB and five transgenic strains: *Tg(XlEef1a1:mlsEGFP)*, *Tg(fli1a:EGFP)*, *Tg(gfap:EGFP)*, *Tg(elavl3:EGFP)*, and *Tg(mbp:EGFP)*. Among these, *Tg(gfap:EGFP)* was obtained from Nanjing Hunter Biotechnology Co., Ltd. (Nanjing, China), while the other four strains were supplied by the National Aquatic Biological Resource Center (Wuhan, China). All zebrafish were maintained at Wenzhou Medical University under standard laboratory conditions in accordance with guidelines approved by the Institutional Animal Care and Use Committee (approval ID: xmsq2022-0302). The transgenic line *Tg(XlEef1a1:mlsEGFP)* expresses mitochondria-localized EGFP, enabling studies of apoptosis and mitochondrial physiology [22]. *Tg(fli1a:EGFP)* labels cranial neural crest derivatives and blood vessels [23]. *Tg(gfap:EGFP)* marks astrocytes and retinal Müller glial cells [24]. *Tg(elavl3:EGFP)* drives fluorescent expression in developing neurons [25]. *Tg(mbp:EGFP)* labels myelinating, mature oligodendrocytes and Schwann cells of zebrafish [26]. Detailed information regarding breeding procedures and embryo collection is provided in the Supplementary Material.

2.2. Characterization of PS under co-exposure with 6PPD

Unlabeled or fluorescence-labeled PS with average diameters of 80 nm (CAS: 6-1-0008; 7-1-0008, 2.5% w/v) were purchased from the Base Line Chrom Tech Research Centre (Tianjin, China). 6PPD (CAS: 793-24-8, purity: >98.0%) was purchased from Tanmo Quality Control Technology Co., Ltd. (Changzhou, China). The characterization of PS under co-exposure with 6PPD was conducted as previously described [27]. Scanning electron microscopy, water contact angle measurements, hydrodynamic size, polydispersity index (PDI), zeta potential, and Fourier transform infrared spectroscopy (FTIR) analyses were conducted, with full methodological details provided in the Supplementary Material.

2.3. PS and 6PPD embryonic co-exposure and developmental evaluations

We performed cute embryonic co-exposures using environmentally relevant concentrations of PS (1 mg L^{-1}) [28] and 6PPD (0.1, 0.4, and 0.8 mg L^{-1}) [21]. Specifically, the 6PPD stock solutions were prepared by dissolving them in 100% dimethyl sulfoxide (DMSO) and stored at −80 °C. We then prepared working exposure solutions by serial dilutions to achieve a final DMSO concentration of 0.1%. The negative control embryos also received 0.1% DMSO (v/v in embryo medium). The PS solutions and 6PPD co-exposure solutions were freshly prepared and sonicated for 20 min before use. Embryos were exposed to different treatment groups from 8 to 120 hpf, a window that encompasses early eye morphogenesis [18], in six-well plates containing 5 mL of solution (20 embryos per well; three replicates per group). We assessed embryonic development by measuring the hatching rate at 60 hpf, pigment formation at 72 hpf, and malformation and mortality rates at 120 hpf. At 120 hpf, we counted the representative malformed larvae and acquired dorsal view images of the head to measure the eye area (EA), retinal pigment area (RPA), exophthalmos length (EL), eye diameter (ED), and axial length (AL); we then calculated the AL/ED ratio as described previously [21].

2.4. Cell death and histopathology evaluations

We evaluated early-stage cell death at 48 hpf using acridine orange (AO) staining and visualized it under a macro zoom fluorescence microscope (OLYMPUS/MVX10, Tokyo, Japan). We then quantified the number of AO-positive cells in the embryonic eye region; details are provided in the Supplementary Material. For histopathological observation, 120 hpf larvae were fixed in 4% paraformaldehyde (PFA) overnight. Subsequent steps included dehydration through a graded ethanol series (70–100%), clearing in xylene, embedding in paraffin, and sectioning at a thickness of 4–5 μm. Light microscopic analysis was conducted on hematoxylin and eosin (H&E)-stained sections. In addition, we prepared frozen sections for apoptosis detection in 120 hpf larvae using terminal deoxynucleotidyl transferase dUTP nick-end labeling (TUNEL). For the staining procedure, we employed diaminobenzidine (DAB) as the chromogenic substrate, and this reaction was catalyzed by streptavidin-conjugated horseradish peroxidase (SA-HRP). The TUNEL kit (G1507-100T) was purchased from Wuhan Servicebio Technology Co., Ltd. (Wuhan, China). Detailed procedures are provided in the Supplementary Material.

2.5. Embryonic behaviors and larval phototaxis evaluations

We evaluated the early-stage behaviors of embryo spontaneous movement, touch response, larval activity, and larval phototaxis. We recorded spontaneous movement of embryos (alternating tail

bending or coiling) at 24 hpf for 1 min using a charge-coupled device camera (Nikon, Japan) mounted on a dissecting microscope. At 48 hpf, we manually dechorionated the embryos and evoked movement by touching the dorsal tail region with an eyelash probe; we then scored the distance moved after touching semi-quantitatively. At 72 hpf, we quantified the locomotor activity of early-hatched larvae using a 10-min free-swimming tracking test, as previously described [29], with detailed methods provided in the Supplementary Material. Larval phototaxis was evaluated at 9 days post-fertilization (dpf) following our previous protocol [30]. Briefly, a two-chamber rectangular apparatus (dark and light zones separated by a sliding partition) was used to assess the phototactic response of groups of 15 larvae. After a 1-min dark adaptation, we lifted the partition and recorded larval swimming toward the light chamber. The assay used a 6PPD concentration of 0.1 mg L^{-1}.

2.6. Confocal imaging of transgenic embryos

To visualize in vivo PS deposition and validate cellular responses in the visual system, transgenic zebrafish embryos were exposed to 0.1% DMSO (Control), 1 mg L^{-1} PS, 0.4 mg L^{-1} 6PPD, or a mixture of both (Mix). We then performed confocal imaging at 120 hpf using a laser confocal C2-2 (Nikon Instruments Inc., Tokyo, Japan). We obtained consecutive Z-stack images to determine PS particle localization within retinal tissues. We quantified morphological and molecular changes across several transgenic lines to assess tissue-specific responses. In the *Tg(XlEef1a1:mlsEGFP)* line (mitochondrial marker), we measured lens size (area) and mlsEGFP expression as indicators of lens development. Lateral imaging of the *Tg(fli1a:EGFP)* line revealed changes in head vasculature, which we quantified by EGFP intensity. Similarly, we quantified fluorescence in *Tg(gfap:EGFP)* (Müller glia), *Tg(elavl3:EGFP)* (neurons), and *Tg(mbp:EGFP)* (oligodendrocytes and Schwann cells) to evaluate the integrity of these neural cell populations.

2.7. 6PPD content analysis

We measured the 6PPD level in 120 hpf larvae after exposure to the Control, 1 mg L^{-1} PS, 0.4 mg L^{-1} 6PPD, or the Mix. For each group, 20 larvae were collected as a single biological replicate (three replicates per treatment) after thorough rinsing in embryo medium. Samples were homogenized in 0.6 mL acetonitrile and 0.3 mL NaCl (1 mol L^{-1}). Homogenates were sonicated for 20 min and centrifuged at 3000 rpm for 10 min; this extraction step was repeated once. The combined extracts were concentrated to near dryness, dissolved in 0.5 mL methanol, and filtered through a 0.22 μm poly (ether sulfone) membrane. Quantification was performed using an AB Sciex 6500 triple-quadrupole tandem mass spectrometer (Applied Biosystems, Foster City, CA, USA) coupled to a Nexera-XZ UPLC system (Shimadzu Corporation Inc., Kyoto, Japan). A standard calibration curve (0.1–50 ng mL^{-1}) was used for 6PPD quantification, yielding the regression equation $y = 1.001x - 0.0069$ ($R^2 = 0.999$, $n = 3$) with an average recovery of 98.2 ± 3.4%. We performed quality assurance and quality control using laboratory blanks, as previously described [21,31].

2.8. Transcriptomic and proteomic analyses of the co-exposed larvae

For transcriptomic and proteomic analyses, we collected larval heads at 120 hpf treated with Control, 1 mg L^{-1} PS, 0.4 mg L^{-1} 6PPD, and the Mix. Twenty larvae per sample were pooled into a single biological replicate, with three replicates per treatment. Total RNA and proteins were extracted following standard manufacturer protocols (Hangzhou LC-Bio Technology Co., Hangzhou, China). Transcriptomic sequencing (mRNA-Seq) was performed using Illumina Novaseq™ 6000, and proteomic analysis was conducted using Nano-LC-MS/MS (nanoESI Orbitrap Exploris™ 480, Thermo Fisher Scientific, San Jose, CA, USA). RNA-Seq read quality control results are presented in Supplementary Table S1. The bioinformatics analysis of the two omics was performed using OmicStudio tools (accessible at https://www.omicstudio.cn/tool). A combined transcriptomic and proteomic analysis was performed. The STRING database (https://string-db.org, version 10.5) was employed to analyze and illustrate the protein–protein interaction (PPI) pathways. Furthermore, we performed gene ontology (GO) enrichments, Kyoto Encyclopedia of Genes and Genomes (KEGG) pathways, and Gene Set Enrichment Analysis (GSEA) using the edgeR package, with a significance cutoff of $P < 0.05$. Detailed procedures are provided in the Supplementary Material.

We conducted an integrative network analysis of gene–protein correlations to elucidate pathways affected by co-exposure, integrating transcriptomic and proteomic datasets. Proteomic identifiers (UniProt IDs) were mapped to transcriptomic gene IDs using a dedicated mapping module. Correlation analysis was conducted using the Hmsic R package, applying thresholds of Rho > 0.3 and $P < 0.05$ to identify significantly correlated gene–protein pairs. Differentially expressed genes and proteins were analyzed using a nine-quadrant method, and associated GO and KEGG enrichment pathways were examined to characterize biological responses to PS/6PPD co-exposure.

2.9. Quantitative real-time PCR validation

We collected larval head tissues from the Control, 0.4 mg L^{-1} 6PPD, and Mix groups at 120 hpf for quantitative real-time PCR (qPCR) validation. The PS group did not show significant differential expression in the target genes. Each biological replicate consisted of pooled head tissues from 20 larvae, with three replicates per group. All oligonucleotide primers (Supplementary Table S2) were synthesized (Shanghai Saiheng Biotechnology Co, Ltd. Shanghai, China). Detailed experimental procedures are provided in the Supplementary Materials.

2.10. Enzyme-linked immunosorbent assay

Oxidative stress and inflammation response were evaluated using enzyme-linked immunosorbent assay (ELISA) kits (Shenzhen Ziker Biological Technology Co., Ltd., Shenzhen, China). We evaluated the oxidative stress markers of the reactive oxygen species (ROS, ZK-F6253), lipid peroxidation indicator malondialdehyde (MDA, ZK-F6255), and glutathione peroxidase 4 (Gpx4, ZK-F8240). For each treatment group (Control, 0.4 mg L^{-1} 6PPD, and Mix), head tissues from 20 larvae at 120 hpf were pooled into a single sample. Each pooled sample was homogenized with a tissue homogenizer using phosphate buffer (pH = 7.4). The homogenate was centrifuged at 6800×*g* for 15 min at 4 °C. Total protein was measured using a BCA assay kit (Nanjing Jiancheng Biological Co. Ltd., Nanjing, China). We performed all assays according to the manufacturer's protocols and quantified sample proteins using standard curves ($R^2 > 0.99$).

2.11. Statistical analysis

We used normality and lognormality tests to assess data distribution. For residuals follow a Gaussian distribution ($\alpha > 0.05$), differences between treatment groups and the Control were analyzed by an ordinary one-way analysis of variance followed by

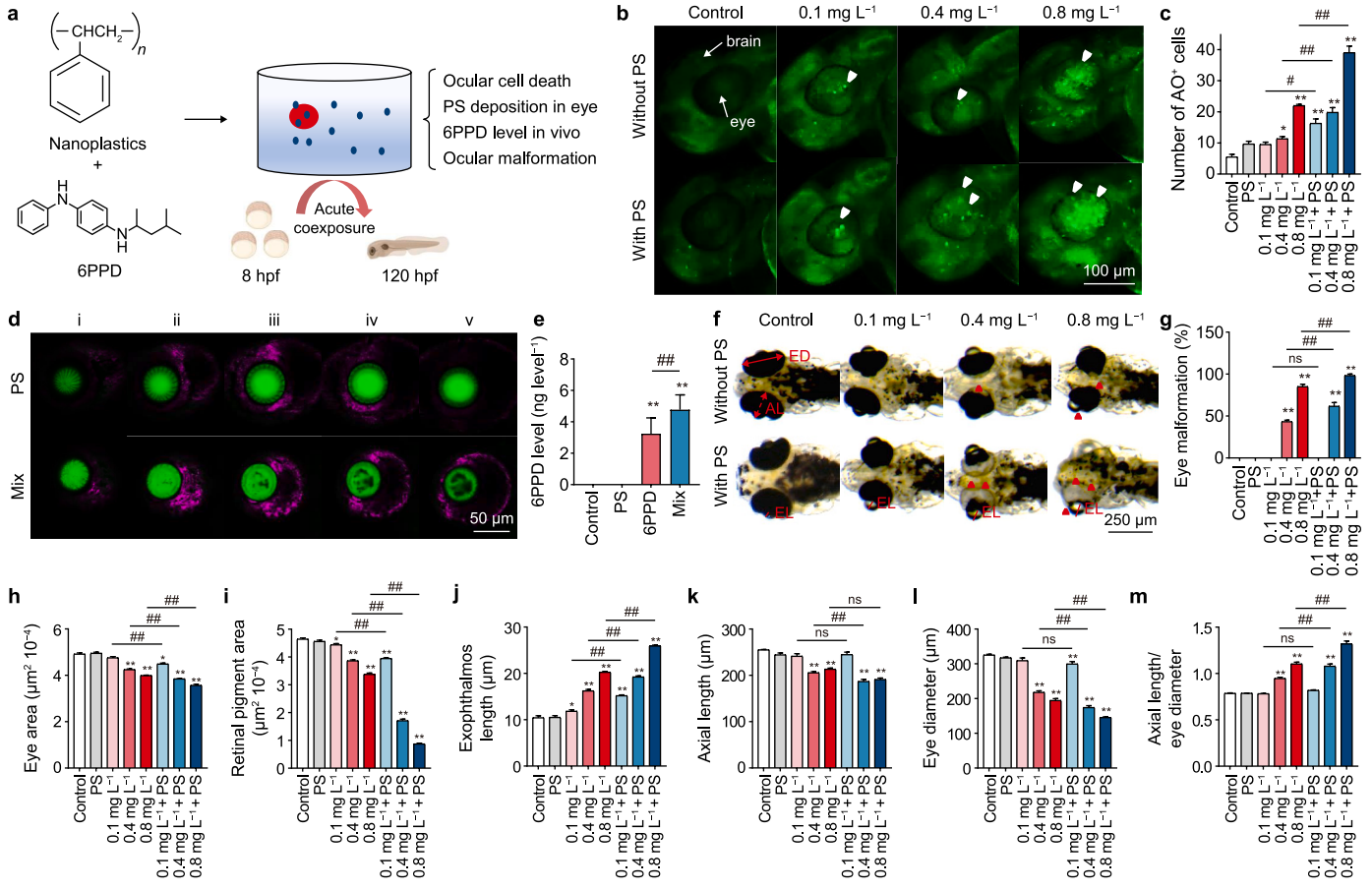

Fig. 1. Embryo ocular toxicity induced by co-exposure to polystyrene (PS) particles and 6PPD. Embryos were continuously exposed from 8 to 120 h post fertilization (hpf) to 0.1% dimethyl sulfoxide (Control), PS (1 mg L^{-1}), 6PPD (0.1, 0.4, and 0.8 mg L^{-1}), or PS + 6PPD (Mix). **a**, Experimental schematic. **b**, Representative acridine orange (AO) staining. Angles point to the death of AO $^{+}$ cells. **c,** Quantification of AO^{+} cells in the eye region at 48 hpf (n = 5–8 embryos per group). **d,** PS particle distribution across the depth of the larval retina; panels i–v show consecutive optical sections (z-stack) acquired at a 10 μm interval. Green, *Xlef1a1*; purple, PS particles. **e,** Quantification of 6PPD in larvae (n = 3 independent samples). **f,** Representative vertical views of larval malformations. Angles point to the malformed eye. ED, eye diameter; AL, axial length; EL, exophthalmos length. **g,** Incidence of eye malformations at 120 hpf (n = 3 independent experiments; 20 individuals per experiment). **h–m,** Eye morphometrics at 120 hpf: eye area (EA, **h**), retinal pigment area (RPA, **i**), exophthalmos length (EL, **j**), AL (**k**), ED (**i**), and AL/ED (**m**) (n = 15 individuals per group). Statistical significance: * $P < 0.05$; ** $P < 0.001$ versus controls; ^{ns}, $P > 0.05$, $^{\#}$ $P < 0.05$, $^{\#\#}$ $P < 0.001$ between the indicated groups.

Tukey's multiple comparisons. Non-normal data ($\alpha < 0.05$) were analyzed using the nonparametric Kruskal–Wallis test followed by Dunn's multiple comparisons test. Analyses were conducted using GraphPad Prism 10.0 (San Diego, CA, USA). Characterization assays for hydration particle size, zeta potential, and PDI were conducted using a one-sample t-test. All data are reported as means ± standard error.

3. Results

3.1. PS particles aggravated 6PPD-Induced zebrafish embryonic ocular toxicity

When combined with the 6PPD water solution, the surface structure of PS became uneven, with irregular, carved shapes (Supplementary Fig. S1a). The water contact angle of the Mix group was significantly lower than that of the PS group (Supplementary Fig. S1b). The Mix also showed significant increases in both hydrodynamic diameter (from 110.3 ± 2.5 nm to 118.7 ± 2.1 nm; $P < 0.05$) and zeta potential (from −18.0 ± 0.26 mV to −15.3 ± 1.45 mV; $P < 0.05$) relative to PS (Supplementary Fig. S1c). The FTIR spectral peaks of the Mix were similar to those of PS but distinct from 6PPD, exhibiting only slight peak shifts (Supplementary Fig. S1d). Thus, the PS nanoplastics from the Mix group exhibited aged-MNP characteristics—porous structure and altered chemical properties—which may affect the surrounding compound, 6PPD.

By adding PS particles to the 6PPD waterborne solutions, the co-exposure counterpart groups showed enhanced embryonic ocular toxicity compared with the 6PPD single groups (Fig. 1a). The co-exposures suppressed the embryo hatching rate (Supplementary Fig. S2a) and significantly increased embryo malformation (Supplementary Fig. S2b) and mortality rates (Supplementary Fig. S2c). Co-exposure significantly suppressed embryo pigment formation (Supplementary Fig. S2d and e). In addition, PS aggravated the suppression of early-stage behaviors induced by 6PPD, including spontaneous movement (Supplementary Fig. S2f), touch response (Supplementary Fig. S2g), and larval activity (Supplementary Fig. S2h). Specifically, co-exposure significantly increased cell death in the embryo eye, with higher AO^{+} cell death in the Mix than in the 6PPD counterpart (Fig. 1b and c). Under confocal imaging, we observed PS particles distributed in the embryo's yolk, eye, brain, and viscera (liver, intestine, swim bladder), with the most accumulation in the eye (Supplementary Fig. S3). Specifically, PS was clustered in the retina, and the deposition depth in the Mix group was larger than that in the PS group (Fig. 1d). Concurrent mass spectrometer analysis revealed that the 6PPD level in the larvae was significantly increased in the Mix compared

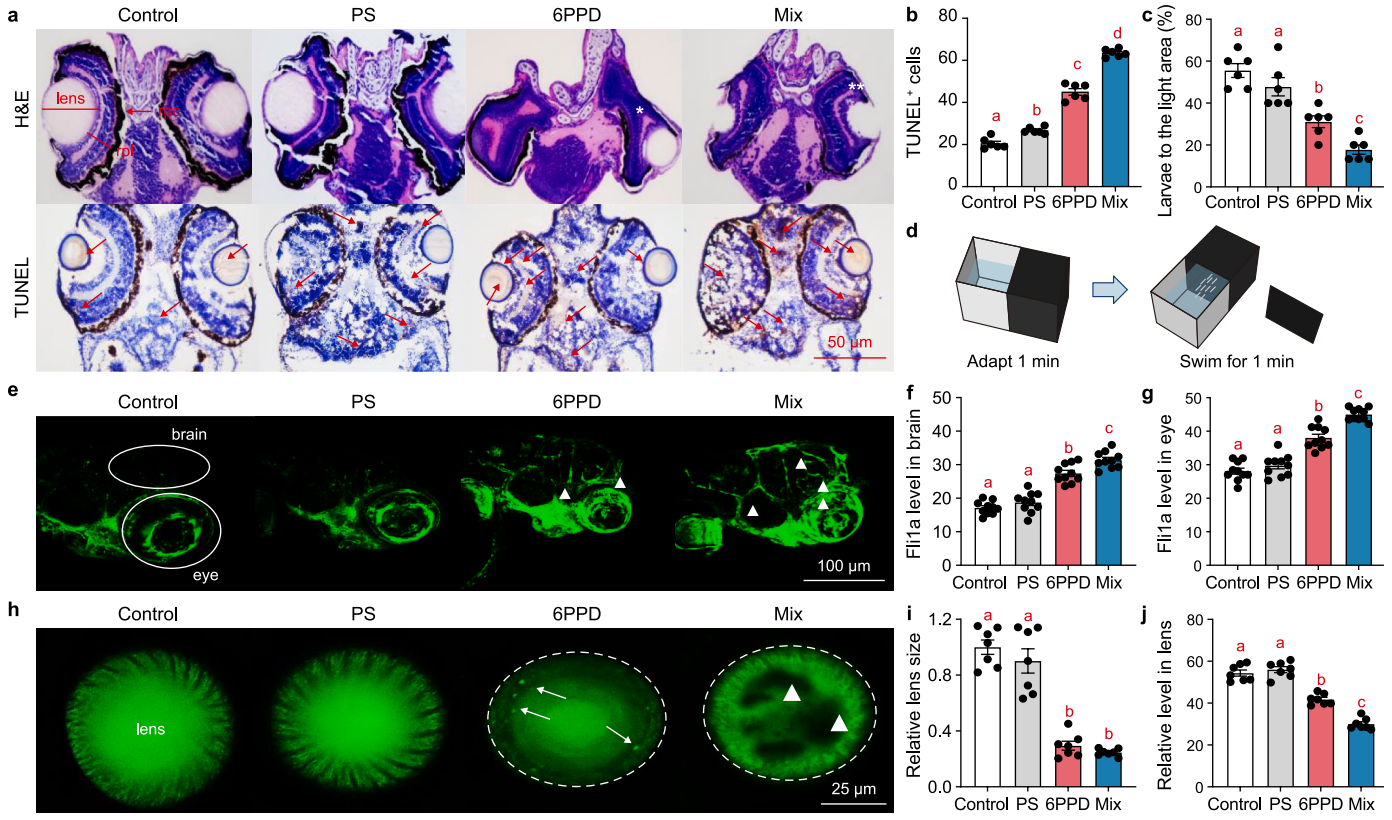

Fig. 2. Effects of PS and 6PPD co-exposure on visual function and eye structure in zebrafish larvae. Embryos were continuously exposed from 8 to 120 h post fertilization (hpf) to 0.1% dimethyl sulfoxide (Control), PS (1 mg L^{-1}), 6PPD (0.1, 0.4, and 0.8 mg L^{-1}), or PS + 6PPD (Mix). **a**, Representative hematoxylin and eosin (H&E) and TUNEL staining of the larval head region. Asterisk, distorted lens border; arrows, TUNEL-positive cells. **b**, Quantification of the TUNEL-positive cells in the head region ($n = 6$). **c**, Phototaxis behavior at 9 days post-fertilization, expressed as the percentage of larvae entering the light chamber ($n = 6$ trials with 15 larvae per trial). **d**, Schematic of the phototaxis assay. **e**, Representative lateral view of the larval head in *Tg(fli1a:EGFP)* embryos; triangles indicate regions with increased Fli1a signal. **f–g**, Quantification of Fli1a fluorescence in the brain (**f**) and eye (**g**) regions ($n = 10$ larvae). **h**, Representative lens morphology in *Tg(XlEef1a1:mlsEGFP)* embryos. Arrows point to apoptotic cells, triangles demarcate lesions, and dashed circles outline regions with disrupted boundaries. **i–j**, Lens **(i)** and intra-lens **(j)** area EGFP fluorescence area measurements ($n = 7$). rpe: retinal pigment epithelium; rpc, retinal photoreceptor layers. Groups sharing the same letter are not significantly different ($P < 0.05$).

to 6PPD (Fig. 1e). The co-exposure obviously induced eye malformations (Fig. 1f). The incidences of eye malformation in the 0.4 and 0.8 mg L^{-1} 6PPD groups were 43.3 ± 2.9% and 85.0 ± 5.0%, respectively, which significantly increased to 61.7 ± 7.6% ($P < 0.001$) and 98.3 ± 2.9% ($P = 0.002$) in the 0.4 mg L^{-1}+PS and 0.8 mg L^{-1}+PS groups (Fig. 1g). Specifically, 6PPD induced a myopia phenotype, as evidenced by measurements of eye size (Fig. 1h–m). Eye area and retinal pigment area were both decreased under co-exposure, with significance starting at 0.4 mg L^{-1} of 6PPD and 0.1 mg L^{-1} Mix, and the decreases were smaller in the Mix groups than in their 6PPD counterparts ($P < 0.001$, Fig. 1h and i). However, the EL was significantly increased in the 6PPD groups ($P < 0.05$ at 0.1 mg L^{-1}, and $P < 0.001$ at higher), which was even bigger in the corresponding Mix groups ($P < 0.001$, Fig. 1j). At the same time, the AL was significantly decreased in the 0.4 and 0.8 mg L^{-1} 6PPD groups ($P < 0.001$), which was even smaller in the corresponding Mix groups ($P < 0.001$, Fig. 1k). The ED was significantly decreased in the 6PPD (0.4 and 0.8 mg L^{-1}) and all the Mix groups ($P < 0.001$, Fig. 1l). However, the AL/ED ratio saw a significant increase starting from the 0.4 mg L^{-1} groups ($P < 0.001$), with the Mix group showing a significantly higher ratio than the single exposure group ($P < 0.001$, Fig. 1m).

3.2. PS enhanced 6PPD-Induced embryonic eye dysfunctions

H&E staining validated aberrant eye structure in the 6PPD and Mix groups, inducing retinal layer abnormalities and lens smear (Fig. 2a). TUNEL staining of OCT-embedded head tissue revealed significant apoptosis in the brain and retina regions, with the Mix group showing the highest positivity (Fig. 2a and b). We manually counted the larval phototactic response and found the percentage of larvae swum to the light chamber was significantly reduced in both the 6PPD and Mix groups, with the Mix group showing a significantly lower percentage compared to the 6PPD group (Fig. 2c and d). Concurrently, enhanced vascular (*Tg(fli1a:EGFP)*) expression in the brain and eye regions was observed in the 6PPD and Mix groups larvae (Fig. 2e–g). Using *Tg(XlEef1a1:mlsEGFP)* to label the mitochondria, we observed that the lens structure in the PS group was similar to that of the Control; however, the lens in the 6PPD and Mix groups exhibited a decrease in size and expression level, as well as disordered surrounding shapes with obvious apoptosis (Fig. 2h–j). The Mix group showed more severe lens damage than the 6PPD group, with obvious necrosis in the central area.

To further investigate neuroglial and myelination alterations under 6PPD/PS co-exposure, we analyzed the fluorescent expression of *Tg(gfap:EGFP)*, *Tg(elavl3:EGFP)*, and *Tg(mbp:EGFP)* (Fig. 3a–c). Specifically, both 6PPD and Mix exposure induced abnormal Müller glia in the larval head and retinal tissues (Fig. 3a), as visualized Gfap expression in the Mix group showing the most pronounced changes (Fig. 3d and e). In addition, co-exposure synergistically activated neurogenesis in the larval head (Fig. 3b),

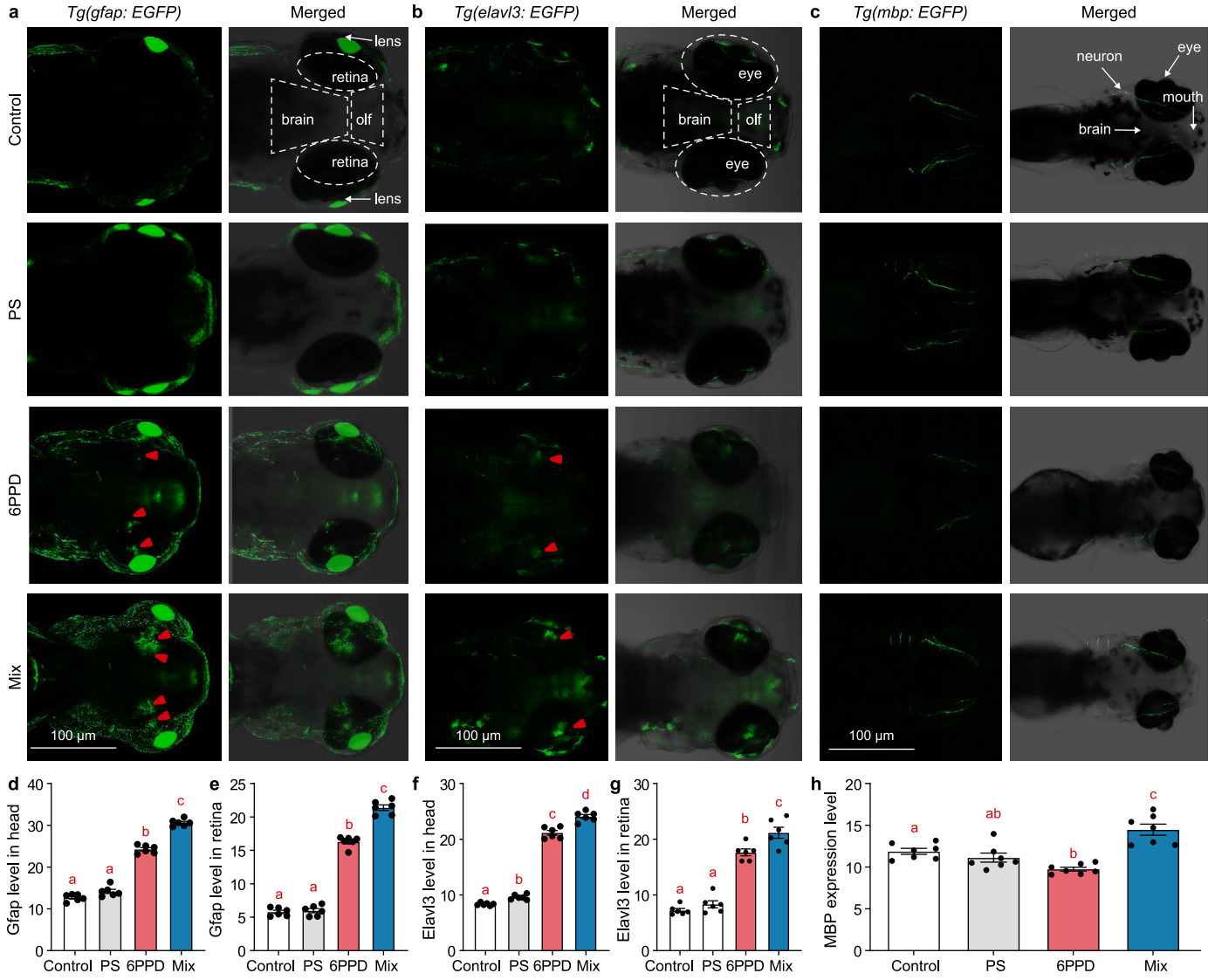

Fig. 3. The impact on the larval eye and visual nerve development under PS/6PPD co-exposures. a–c, Confocal vertical larval heads of the transgenic strains of *Tg(gfap: EGFP)* **(a)**, *Tg(elavl3: EGFP)* **(b)**, and *Tg(mbp: EGFP)* **(c),** shown as the channel of single GFP and merged views, with the GFP signal superimposed on a bright-field background. **d–e**, Quantification of the Gfap level in the whole head **(d)** and retina **(e)** regions ($n = 6$). **f–g**, Quantification of the expression level of the Elavl3 in the whole head **(f)** and eye **(g)** regions ($n = 6$). **h**, Quantification of the Mbp expression level ($n = 7$). olf: olfactory. Arrowheads indicate regions with increased fluorescence. Groups sharing the same letter are not significantly different ($P < 0.05$).

particularly in the eye region, as revealed by the Elavl3 reporter (Fig. 3f and g). Furthermore, analysis using the *Tg(mbp:EGFP)* line showed that Mbp expression was significantly decreased in the 6PPD group but increased in the Mix group compared with controls (Fig. 3c–h).

3.3. PS and 6PPD co-exposure altered the larval transcriptomics and proteomics

To elucidate the molecular mechanisms underlying the developmental ocular toxicity induced by co-exposure to PS and 6PPD in zebrafish, we performed integrated transcriptomic and proteomic analyses of larval head tissues. mRNA-Seq and proteomics were applied to assess the impacts of co-exposure on gene expression and protein profiles, respectively (Fig. 4).

At the transcriptomic level, Pearson correlation analysis revealed high internal consistency among samples, with correlation coefficients ranging from 0.66 to 0.99 (Supplementary Fig. S4a). Heatmap clustering showed that gene expression patterns in the 6PPD and Mix groups were markedly similar, whereas those of the PS group diverged substantially from both (Supplementary Fig. S4b). Venn diagram analysis further demonstrated that although the PS group exhibited a larger number of differentially expressed genes, the overlap between the 6PPD and Mix groups was greater than that between PS and Mix or between PS and 6PPD (Fig. 4a). GO enrichment analysis highlighted distinct functional perturbations among exposure groups. The 6PPD and Mix groups were predominantly enriched for biological processes associated with visual perception, phototransduction, and cellular response to unfolded proteins (Fig. 4b and c), all of which are tightly linked to eye development. In contrast, the PS group was enriched for processes related to muscle contraction and sarcomere organization (Supplementary Fig. S4c), suggesting a fundamentally different mode of action. Notably, 6PPD exposure additionally enriched GO terms associated with G protein-coupled receptor (GPCR) kinase activity and protein folding/misfolding,

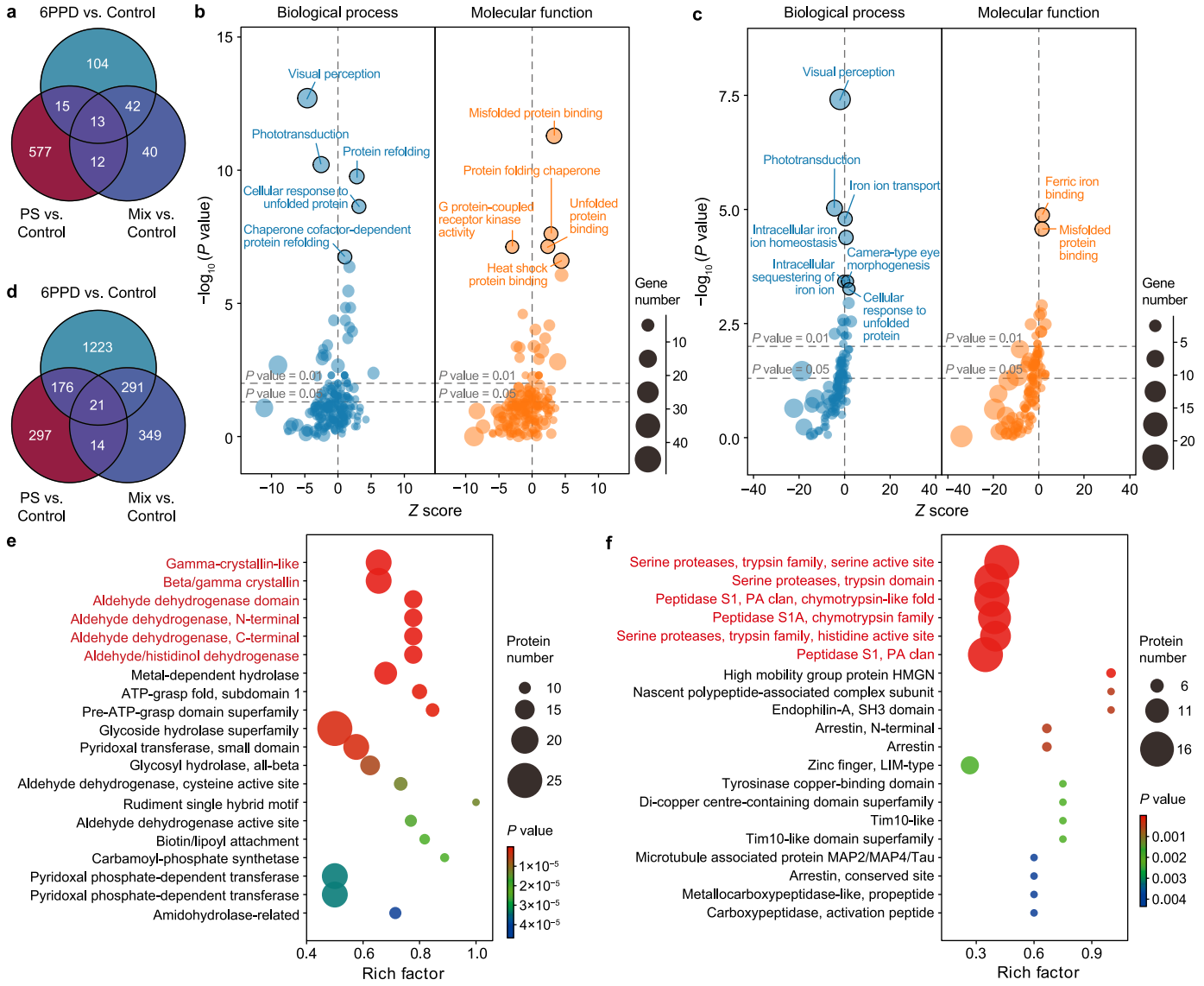

Fig. 4. Co-exposure impacted transcriptomic and proteomic expression in larvae at 120 h post fertilization. a, Venn diagram analysis of the genes. **b–c,** Gene ontology enrichment of differentially expressed genes in the 6PPD (**b**) and PS + 6PPD (Mix, **c**), shown as bubble plots. **d,** Venn diagram analysis of the proteins. **e–f,** InterPro (protein domain) enrichment of differentially expressed proteins in the 6PPD (**e**) and Mix (**f**), shown as scatter plots.

whereas the Mix group uniquely enriched iron ion transport and homeostasis, iron binding, camera-type eye morphogenesis, and the dynactin complex (Fig. 4b and c). Additionally, GSEA-based GO enrichment revealed no visual function–related genes in the PS group (Supplementary Fig. S5a), while 4 and 6 items were identified in the 6PPD and Mix group, respectively (Supplementary Fig. S5b and c).

At the proteomic level, Pearson correlations ranged from 0.82 to 1.00 across samples (Supplementary Fig. S4d), supporting dataset reliability. Proteomic heatmaps revealed clustering patterns consistent with transcriptomic findings, with the 6PPD and Mix groups being highly similar, whereas the PS group was distinctly separated (Supplementary Fig. S4e). Venn analysis further showed that the number of differentially expressed proteins was highest in the 6PPD group, and the proportion shared between the 6PPD and Mix groups exceeded that shared with PS (Fig. 4d), reinforcing the similarity between 6PPD and co-exposure responses at the protein level. Concurrent enrichment in protein domains for the 6PPD group was related to lens and retinoic acid metabolism, such as gamma crystallin-like, beta/gamma crystallin, and aldehyde dehydrogenases, which were proteases for serine, trypsin, and peptides in the Mix group (Fig. 4e and f). In contrast, the top protein domains in the PS group were armadillo-type fold/helical, Fe^{2+} dioxygenase domain, and so on (Supplementary Fig. S4f). The protein GSEA_GO analysis showed similar changes with zero, five, and seven items in the PS, 6PPD, and Mix groups (Supplementary Fig. S5d–f).

3.4. PS and 6PPD co-exposure altered the transcriptome and proteomics in larvae

The combined omics analyses further explored the molecular mechanisms of visual dysfunction exacerbation due to co-exposure (Fig. 5). The Spearman correlation coefficient for the two omics was symmetrically distributed with a median of −0.03 (Fig. 5a). The nine-quadrant analysis, coupled with the GO and KEGG enrichment analysis, showed variant enrichment for the three treatment groups (Fig. 5b and c, Supplementary Fig. S6a–c).

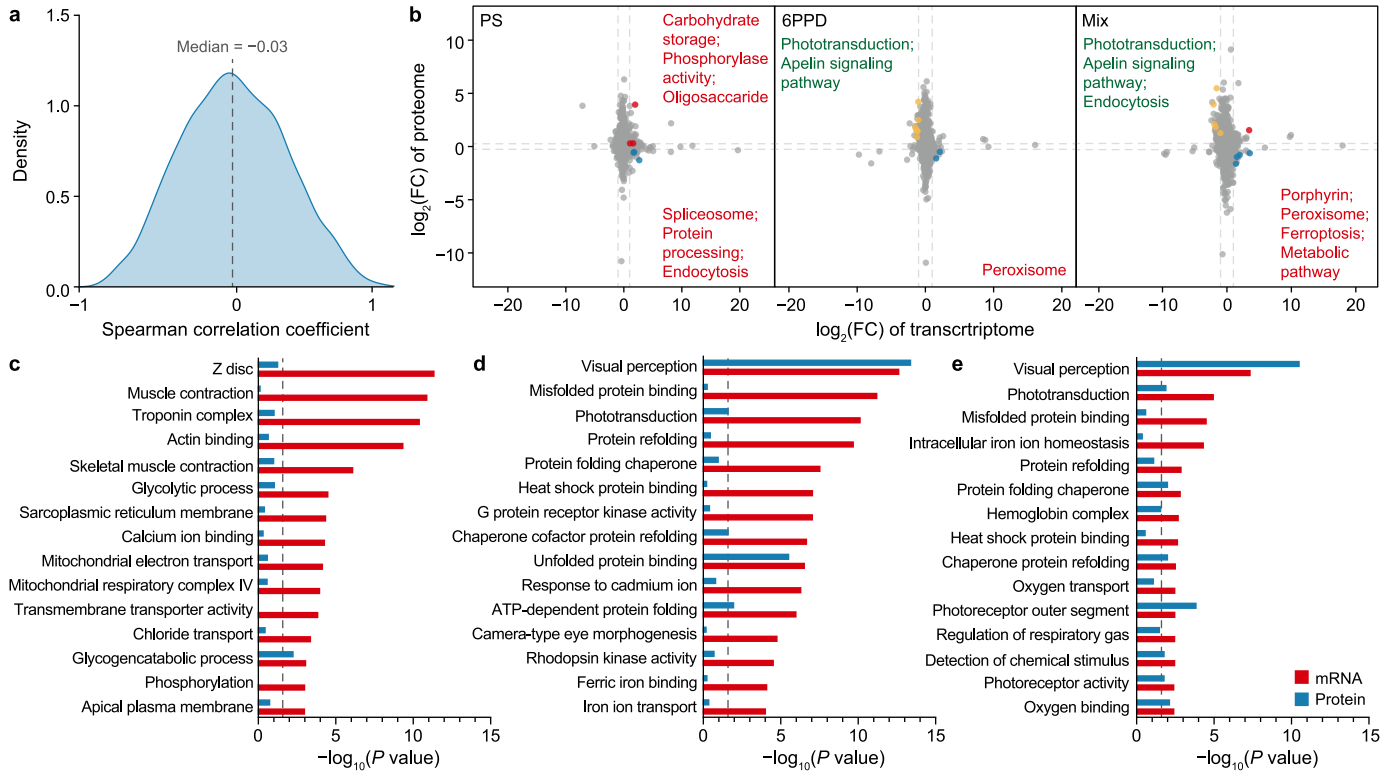

Fig. 5. Combined transcriptome and proteome analysis for PS/6PPD-induced enhanced visual toxicity. a, T Distribution of pairwise correlation coefficients between transcriptome and proteome measurements. **b**, Nine-quadrant plot showing concordance and discordance between differential expression at the mRNA and protein levels for the PS80, 6PPD, and PS + 6PPD (Mix) groups. Grey, features not significantly different in either omics dataset (both fold-change [FC] and *P*-value thresholds were not met in both datasets); red, significantly upregulated in both transcriptomics and proteomics; blue, significantly upregulated in transcriptomics but significantly downregulated in proteomics; yellow, significantly downregulated in transcriptomics but significantly upregulated in proteomics. Enriched terms are annotated in the corresponding quadrants, with red denoting the upregulated terms and green denoting the downregulated terms. **c–e,** Top 20 gene ontology terms enriched among the overlapping differentially expressed features identified in the transcriptome–proteome intersection for PS80 **(c)**, 6PPD **(d)**, and Mix **(e)** groups. The dashed line denotes $P = 0.05$.

PS enrichment was less common than in the 6PPD or Mix groups; however, the latter two groups showed altered visual responses. In detail, in the gene-down protein-up quadrant, phototransduction and apelin signaling pathway were affected by both 6PPD and Mix treatments, with the latter also affecting endocytosis; in the gene-up protein-down quadrant, peroxisomes were affected by both 6PPD and Mix treatments, with the latter also affecting porphyrin metabolism, ferroptosis, and metabolic pathways; in the gene-up protein-up quadrant, only the Mix group affected the hemoglobin complex, oxygen transport, oxygen binding, and heme binding (Fig. 5b). The top dual GO enrichment indicated that there were no genes related to vision in the PS treatment (Fig. 5c); however, visual perception, phototransduction were found in the 6PPD and Mix groups (Fig. 5d and e). Besides, G protein receptor kinase activity and camera-type eye morphogenesis were found in the 6PPD group (Fig. 5d), and photoreceptor outer segment and photoreceptor activity were found in the Mix group (Fig. 5e). In addition, changes were observed in intracellular iron ion homeostasis, hemoglobin complex, oxygen transport, regulation of respiratory gas, and oxygen binding in the Mix group (Fig. 5e). In agreement with the dual GO analysis, the top dual KEGG enrichment was phototransduction for both the 6PPD and Mix groups; the second enrichment for Mix was ferroptosis (Supplementary Fig. S6b and c).

3.5. PS and 6PPD co-exposure aggravated visual dysfunctions via ferroptosis

Further PPI gene networks were constructed for the 6PPD and Mix groups (Fig. 6a and b). In detail, both 6PPD and Mix groups induced eye dysfunction by suppressing the expression of visual genes and apelin signaling genes, *gnb3a* and *gnb3b*. 6PPD treatment affected the crosstalk genes of *gnat1/2* linking with peroxisome signaling (*prdx1*, *hmox11a*) (Fig. 6a). However, the Mix treatment affected more crosstalk genes of *opn1mw1*, *opn6b*, *rlbp1b*, *gnat2*, and *pde6a*, which in turn induced more complicated gene expression involved in peroxisome, ferroptosis (*fthl27/28/31*, *gpx9*, *gstp1/2*), and endocytosis (*hsp70.2/3*, *unc119*, *unc119b*) (Fig. 6b).

From both the RNA-Seq and qPCR, the genes of ferritin, heavy polypeptide-like 27 (*fthl27*), and heme oxygenase 1a (*hmox1a*) showed a significant overexpression pattern compared to controls, and the genes of short-wave sensitive 1 (*opn1sw1*) and G protein subunit alpha transducing 2 (*gnat2*) were significantly downregulated compared to controls, exhibiting lower expression levels in the Mix than in the 6PPD group (Fig. 6c and d). In addition, we also examined another three genes using qPCR, and it indicated that G protein subunit alpha transducin 1 (*gnat1*) was significantly decreased more in the Mix than in the 6PPD group (Fig. 6e), while transferrin receptor 1a (*tfr1a*) and hemoglobin, alpha adult 1 (*hbaa1*) were significantly increased in the Mix group as compared to the Control or 6PPD groups (Fig. 6f and g).

To further validate ferroptosis activation and oxidative stress, ELISA assays were performed. Both treatment groups showed a significant increase in ROS levels compared to the controls ($P < 0.001$), with the Mix group having significantly higher ROS levels than the 6PPD group ($P < 0.001$, Fig. 6h). MDA content, a marker of lipid peroxidation, was significantly increased in both

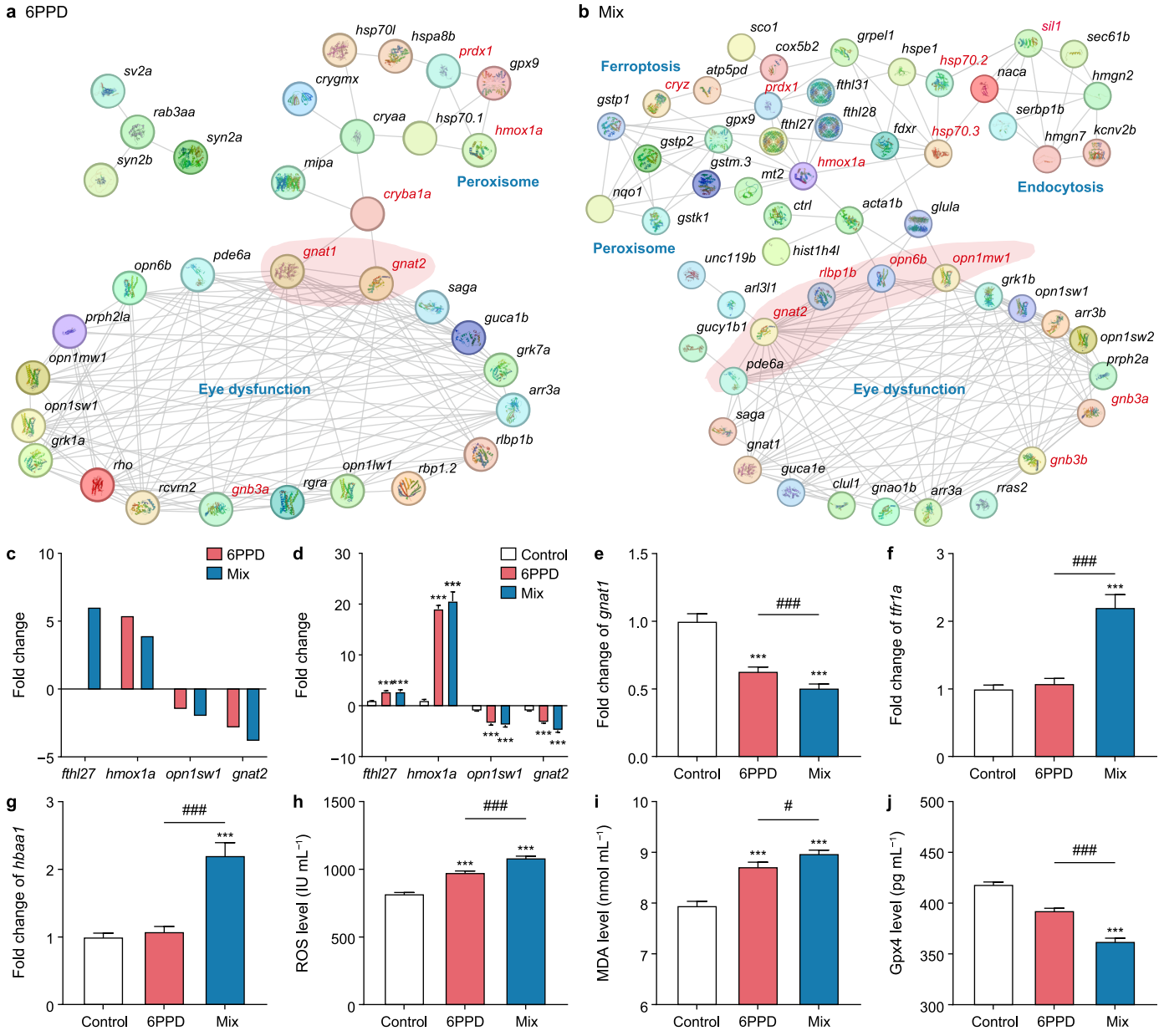

Fig. 6. PS and 6PPD co-exposures aggravated zebrafish eye dysfunctions via ferroptosis. **a**–**b**, Protein–protein interaction (PPI) networks generated using STRING based on integrated transcriptomic and proteomic datasets for the 6PPD (**a**) and PS + 6PPD (Mix, **b**) groups. Bold blue texts indicate enriched terms associated with the linked gene clusters. The red genes denoted the primarily connected ones in the network. A red shadow highlighted the linked genes between eye dysfunction and other pathways. **c**, RNA-seq–derived expression levels of *fthl27*, *hmox1a*, *opn1sw1*, and *gnat2* in the 6PPD and Mix groups. **d**, qPCR validation of selected genes in the Control, 6PPD, and Mix groups ($n = 4$). **e**–**g**, The gene expression level of *gnat1* (**e**), *tfr1a* (**f**), and *hbaa1* (**g**) from qPCR. Gene symbols: ferritin heavy polypeptide-like 27 (*fthl27*), heme oxygenase 1a (*hmox1a*), short-wave sensitive 1 (*opn1sw1*), G protein subunit alpha transducin 1/2 (*gnat2*, *gnat1*), transferrin receptor 1a (*tfr1a*), hemoglobin, alpha adult 1 (*hbaa1*). **h**–**j**, Oxidative stress markers measured by ELISA: reactive oxygen species (ROS, **h**), malondialdehyde (MDA, **i**), and glutathione peroxidase 4 (Gpx4, **j**) ($n = 3$). Statistical significance: $^{***}P < 0.001$ versus control; $^{\#}P < 0.05$ and $^{\#\#\#}P < 0.001$ between the indicated groups.

groups ($P < 0.001$), with the Mix group showing a higher increase than the 6PPD group ($P < 0.05$, Fig. 6i). Gpx4, an antioxidant enzyme, was significantly decreased in both groups ($P < 0.001$), with the Mix group having significantly lower levels than the 6PPD group ($P < 0.001$, Fig. 6j).

4. Discussion and conclusion

4.1. Synergistic potentiation of developmental toxicity

The co-occurrence of MNPs and plastic additives represents a complex toxicological threat to aquatic ecosystems. MNPs are well-documented vectors for hydrophobic contaminants, frequently altering their bioavailability and toxicity [27,32,33]. Our findings confirm that PS nanoplastics significantly potentiate 6PPD-induced developmental toxicity in zebrafish embryos. While phenotypic defects induced by 6PPD alone—such as ocular malformations and reduced pigmentation—align with prior reports [17,21,34], the co-exposure group exhibited a distinct and exacerbated toxicity profile. This included severe myopia-like ocular dysfunction, exophthalmos, and pronounced suppression of phototactic behavior. The synergistic reduction in hatching rates

and survival suggests that single-pollutant assessments may severely underestimate the ecological risks of road runoff mixtures. The exacerbation of these defects correlates strongly with the enhanced bioaccumulation of 6PPD, driven by the physical presence of PS, identifying the nanoplastic as a critical amplifier of chemical toxicity.

4.2. Ocular architecture disruption and neuroglial activation

The synergistic toxicity manifested as severe structural disruption within the ocular tissue. Beyond general apoptosis, the co-exposure triggered specific patterns of cell death and tissue remodeling not seen in single exposures. In vivo imaging (*Tg(XlEef1a1:mlsEGFP)*) revealed precise localization of mitochondrial-dependent apoptosis at the lens margin and necrosis in the central lens, mirroring toxicity patterns of other tire-derived compounds [16]. Besides, we observed exacerbated vascular mispatterning. The abnormal angiogenesis in the co-exposed group suggests that rapid, unregulated vessel growth may impose mechanical stress on the retina, compounding tissue damage [21,35]. Additional transgenic analysis revealed a specific upregulation of Gfap (Müller glia activation) and Elavl3 (post-mitotic neurons) in the retina. While Gfap upregulation typically signals a regenerative response to neuronal injury [36–38], the concurrent downregulation of myelin basic protein (MBP) in the 6PPD-only group—contrasted with its erratic upregulation in the mix group—indicates a chaotic disruption of neural myelination. These findings suggest that co-exposure does not merely kill cells but fundamentally disrupts the neuroglial architecture essential for visual signal processing.

4.3. The "Trojan horse" mechanism: vector effects and bioaccumulation

The exacerbated toxicity is mechanistically driven by the "Trojan horse" effect, where MNPs facilitate the transport of contaminants into biological tissues [39]. Our physicochemical characterization indicated that the PS particles in the co-exposure system underwent aging processes, evidenced by surface microcracks, reduced zeta potential, and altered FTIR spectra. These aging-induced surface modifications typically increase the adsorption capacity for hydrophobic organic contaminants [40–42]. Consequently, the PS nanoplastics served as efficient vectors, penetrating deeper into retinal tissues and significantly elevating the internal body burden of 6PPD compared to waterborne exposure alone. This aligns with findings in *C. elegans*, where nanoplastics enhanced the uptake of 6PPD-quinone [11], confirming that physical adsorption mechanisms are a primary driver of the observed synergistic lethality in zebrafish.

4.4. Dual-omics revelation of visual pathway dysregulation

Integrated transcriptomic and proteomic profiling highlighted a divergence in toxicity mechanisms between single and combined exposures. While 6PPD alone perturbed specific visual proteins (e.g., Crystallins, Aldh1a), the co-exposure elicited a systemic collapse of visual regulation pathways. Specifically, the co-exposure uniquely suppressed key phototransduction genes (*opn1sw1*, *gnat1/2*) and dysregulated GPCR signaling [43,44]. The disruption of Aldh1a implies a failure in retinoic acid synthesis, a critical morphogen for eye development [45,46]. The unique alteration of serine protease activity in the co-exposed group suggests a breakdown in the antioxidant defense system and serine metabolism within the eye [47]. Crucially, pathway analysis revealed that while 6PPD targets specific eye function proteins, the co-exposure broadly dysregulates endocytosis and metabolic homeostasis, creating a more hostile cellular environment that exceeds the embryo's compensatory capacities.

4.5. Ferroptosis as a key driver of ocular damage

Our study identifies ferroptosis as a critical, distinct mechanism driving the toxicity of the PS/6PPD mixture. Unlike the general oxidative stress observed in single exposures, the co-exposure group showed a specific upregulation of iron metabolism regulators (*fth*, *tfr1a*, *hmox1a*, *hbaa1*), which are hallmarks of ferroptotic cell death [48–51]. Environmental pollutants are known to induce ROS; however, the simultaneous suppression of Gpx4 and elevation of MDA levels in the co-exposed larvae indicates a failure of the glutathione-dependent antioxidant system. This suggests that the PS vectors deliver a high dose of 6PPD that overwhelms mitochondrial defenses, transitioning the cell death mechanism from simple apoptosis to a severe, iron-dependent ferroptosis. This mechanistic shift explains the widespread retinal necrosis and functional blindness observed in the co-exposed larvae.

4.6. Conclusion and environmental implications

This study provides robust evidence that PS nanoplastics synergistically amplify the ocular toxicity of the tire antioxidant 6PPD in aquatic vertebrates. Through a "Trojan horse" mechanism, nanoplastics enhance 6PPD bioaccumulation, triggering a cascade of oxidative stress, mitochondrial dysfunction, and ferroptosis that leads to severe visual impairment. The specific loss of visual function has profound ecological implications, as it directly compromises critical survival behaviors such as prey capture and predator avoidance. Given the ubiquity of tire wear particles and microplastics in urban runoff, aquatic species in coastal and riverine habitats are likely facing higher risks than predicted by single-chemical models.

While zebrafish are a robust model, future research must address particle size-dependent effects (e.g., 50 nm vs. 500 nm) and polymer variations to fully map the hazards of plastic-additive complexes. Ultimately, these findings underscore the urgent need to consider co-pollutants in environmental risk assessments for road runoff and plastic pollution.

CRediT authorship contribution statement

Jian Lin: Writing - Original Draft, Data Curation, Conceptualization. **Dongliang Pan:** Data Curation. **Xingxing Chen:** Data Curation. **Minyan Xu:** Formal Analysis, Data Curation. **Yangfan Zhu:** Data Curation. **Yi Zheng:** Data Curation. **Yang Song:** Writing - Review & Editing, Visualization, Resources. **Jiangfei Chen:** Writing - Review & Editing, Writing - Original Draft, Visualization, Supervision, Resources, Methodology, Investigation, Funding Acquisition, Data Curation, Conceptualization.

Declaration of competing interest

The authors declare that they have no known competing financial interests or personal relationships that could have appeared to influence the work reported in this paper.

Acknowledgments

We thank the Scientific Research Center of Wenzhou Medical University for providing excellent consultation and instrumental support. We thank LC-Bio Technology Co., Ltd., Hangzhou, China, especially Shuaitong Chen, for technical assistance with

transcriptome and proteome analysis. This work was supported in part by funding from the Natural Science Foundation of Zhejiang Province (No. ZCLY24B0702), Wenzhou Science and Technology project (No. S2023007), Wenzhou Municipal Key Laboratory of Neurodevelopmental Pathology and Physiology (No. 2023HZSY0003), the Project of South Zhejiang Institute of Radiation Medicine and Nuclear Technology (No. ZFY-2022-K-004) and National Innovation and Entrepreneurship Training Program for College Students (No. S202510343117X).

Appendix A. Supplementary data

Supplementary data to this article can be found online at https://doi.org/10.1016/j.ese.2026.100657.

References

[1] E.C. Emenike, C.J. Okorie, T. Ojeyemi, A. Egbemhenghe, K.O. Iwuozor, O.D. Saliu, H.K. Okoro, A.G. Adeniyi, From oceans to dinner plates: the impact of microplastics on human health, Heliyon 9 (10) (2023) e20440.
[2] G. Cao, W. Wang, J. Zhang, P. Wu, X. Zhao, Z. Yang, D. Hu, Z. Cai, New evidence of rubber-derived quinones in water, air, and soil, Environ. Sci. Technol. 56 (7) (2022) 4142–4150.
[3] J.E. Tamis, A.A. Koelmans, R. Dröge, N.H.B.M. Kaag, M.C. Keur, P.C. Tromp, R.H. Jongbloed, Environmental risks of car tire microplastic particles and other road runoff pollutants, Micropl Nanopl 1 (1) (2021) 10.
[4] C. Rauert, S. Vardy, B. Daniell, N. Charlton, K.V. Thomas, Tyre additive chemicals, tyre road wear particles and high production polymers in surface water at 5 urban centres in Queensland, Australia, Sci. Total Environ. 852 (2022) 158468.
[5] C. Johannessen, P. Helm, C.D. Metcalfe, Detection of selected tire wear compounds in urban receiving waters, Environ Pollut 287 (2021) 117659.
[6] J. Yi, J. Ruan, H. Yu, B. Wu, J. Zhao, H. Wang, R. Chen, Q. Yang, J. Chen, D. Sun, Environmental fate, toxicity, and mitigation of 6PPD and 6PPD-Quinone: current understanding and future directions, Environ Pollut 375 (2025) 126352.
[7] M. Deng, X. Ji, B. Peng, M. Fang, In vitro and in vivo biotransformation profiling of 6PPD-Quinone toward their detection in human urine, Environ. Sci. Technol. 58 (21) (2024) 9113–9124.
[8] N. Rafa, B. Ahmed, F. Zohora, J. Bakya, S. Ahmed, S.F. Ahmed, M. Mofijur, A.A. Chowdhury, F. Almomani, Microplastics as carriers of toxic pollutants: source, transport, and toxicological effects, Environ Pollut 343 (2024) 123190.
[9] J.A. Pitt, J.S. Kozal, N. Jayasundara, A. Massarsky, R. Trevisan, N. Geitner, M. Wiesner, E.D. Levin, R.T. Di Giulio, Uptake, tissue distribution, and toxicity of polystyrene nanoparticles in developing zebrafish (Danio rerio), Aquat. Toxicol. 194 (2018) 185–194.
[10] S.L. Wright, R.C. Thompson, T.S. Galloway, The physical impacts of microplastics on marine organisms: a review, Environ Pollut 178 (2013) 483–492.
[11] X. Hua, D. Wang, Polyethylene nanoparticles at environmentally relevant concentrations enhances neurotoxicity and accumulation of 6-PPD quinone in Caenorhabditis elegans, Sci. Total Environ. 918 (2024) 170760.
[12] Y. Jiang, C. Wang, L. Ma, T. Gao, Y. Wāng, Environmental profiles, hazard identification, and toxicological hallmarks of emerging tire rubber-related contaminants 6PPD and 6PPD-quinone, Environ. Int. 187 (2024) 108677.
[13] J. Zheng, L. He, Q. Shi, M. Wang, Y. Ma, W. Yu, L. Liu, G. Yu, X. Liu, B. Wang, J. Zhong, In vivo and in vitro assessment of the retinal toxicity of polystyrene nanoplastics, Environ. Int. 198 (2025) 109420.
[14] J. Lin, D. Pan, Y. Zhu, B. Shen, Z. Sun, Y. Zheng, Y. Yin, C. Huang, W. Wu, Y. Song, J. Chen, Polystyrene nanoplastics chronic exposure cause zebrafish visual neurobehavior toxicity through TGFβ-crystallin axis, J Hazard Mater 492 (2025) 138255.
[15] J. Chen, Q. Liang, Y. Zheng, Y. Lei, X. Gan, H. Mei, C. Bai, H. Wang, J. Ju, Q. Dong, Y. Song, Polystyrene nanoplastics induced size-dependent developmental and neurobehavioral toxicities in embryonic and juvenile zebrafish, Aquat. Toxicol. 267 (2024) 106842.
[16] J. Chang, R. Huang, Z. Zhang, Y. Pan, Z. Ma, B. Wan, H. Wang, A ubiquitous tire rubber additive induced serious eye injury in zebrafish (Danio rerio), J Hazard Mater 472 (2024) 134461.
[17] S. Varshney, A.H. Gora, P. Siriyappagouder, V. Kiron, P.A. Olsvik, Toxicological effects of 6PPD and 6PPD quinone in zebrafish larvae, J Hazard Mater 424 (Pt C) (2022) 127623.
[18] J. Chhetri, G. Jacobson, N. Gueven, Zebrafish–on the move towards ophthalmological research, Eye (Lond) 28 (4) (2014) 367–380.
[19] J. Bilotta, S. Saszik, The zebrafish as a model visual system, Int. J. Dev. Neurosci. 19 (7) (2001) 621–629.
[20] C.J. Moore, Synthetic polymers in the marine environment: a rapidly increasing, long-term threat, Environ. Res. 108 (2) (2008) 131–139.
[21] S.Y. Zhang, X. Gan, B. Shen, J. Jiang, H. Shen, Y. Lei, Q. Liang, C. Bai, C. Huang, W. Wu, Y. Guo, Y. Song, J. Chen, 6PPD and its metabolite 6PPDQ induce different developmental toxicities and phenotypes in embryonic zebrafish, J Hazard Mater 455 (2023) 131601.
[22] M.J. Kim, K.H. Kang, C.H. Kim, S.Y. Choi, Real-time imaging of mitochondria in transgenic zebrafish expressing mitochondrially targeted GFP, Biotechniques 45 (3) (2008) 331–334.
[23] N.D. Lawson, B.M. Weinstein, In vivo imaging of embryonic vascular development using transgenic zebrafish, Dev. Biol. 248 (2) (2002) 307–318.
[24] R.L. Bernardos, L.K. Barthel, J.R. Meyers, P.A. Raymond, Late-stage neuronal progenitors in the retina are radial müller glia that function as retinal stem cells, J. Neurosci. 27 (26) (2007) 7028–7040.
[25] S. Khuansuwan, L.M. Barnhill, S. Cheng, J.M. Bronstein, A novel transgenic zebrafish line allows for in vivo quantification of autophagic activity in neurons, Autophagy 15 (8) (2019) 1322–1332.
[26] S.H. Jung, S. Kim, A.Y. Chung, H.T. Kim, J.H. So, J. Ryu, H.C. Park, C.H. Kim, Visualization of myelination in GFP-transgenic zebrafish, Dev. Dyn. 239 (2) (2010) 592–597.
[27] J. Chen, Y. Lei, J. Wen, Y. Zheng, X. Gan, Q. Liang, C. Huang, Y. Song, The neurodevelopmental toxicity induced by combined exposure of nanoplastics and penicillin in embryonic zebrafish: the role of aging processes, Environ Pollut 335 (2023) 122281.
[28] F. Xiong, J. Liu, K. Xu, J. Huang, D. Wang, F. Li, S. Wang, J. Zhang, Y. Pu, R. Sun, Microplastics induce neurotoxicity in aquatic animals at environmentally realistic concentrations: a meta-analysis, Environ Pollut 318 (2023) 120939.
[29] J. Chen, R.L. Tanguay, Y. Xiao, D.E. Haggard, X. Ge, Y. Jia, Y. Zheng, Q. Dong, C. Huang, K. Lin, TBBPA exposure during a sensitive developmental window produces neurobehavioral changes in larval zebrafish, Environ Pollut 216 (2016) 53–63.
[30] L. Yang, X. Lu, D. Pan, Y. Zhang, Y. Zheng, H. Mei, B. Yang, D. Sun, Q. Li, J. Lin, J. Chen, 6PPD and 6PPDQ embryonic exposure induced distinct developmental neurotoxicity in zebrafish, Ecotoxicol. Environ. Saf. 300 (2025) 118456.
[31] Y.-J. Zhang, T.-T. Xu, D.-M. Ye, Z.-Z. Lin, F. Wang, Y. Guo, Widespread N-(1,3-Dimethylbutyl)-N′-phenyl-p-phenylenediamine quinone in size-fractioned atmospheric particles and dust of different indoor environments, Environ. Sci. Technol. Lett. 9 (5) (2022) 420–425.
[32] Z. Li, H. Xian, R. Ye, Y. Zhong, B. Liang, Y. Huang, M. Dai, J. Guo, S. Tang, X. Ren, R. Bai, Y. Feng, Y. Deng, X. Yang, D. Chen, Z. Yang, Z. Huang, Gender-specific effects of polystyrene nanoplastic exposure on triclosan-induced reproductive toxicity in zebrafish (Danio rerio), Sci. Total Environ. 932 (2024) 172876.
[33] H. Xian, Z. Li, R. Bai, R. Ye, Y. Feng, Y. Zhong, B. Liang, Y. Huang, J. Guo, B. Wang, M. Dai, S. Tang, X. Ren, X. Chen, D. Chen, X. Yang, Z. Huang, From cradle to grave: deciphering sex-specific disruptions of the nervous and reproductive systems through interactions of 4-methylbenzylidene camphor and nanoplastics in adult zebrafish, J Hazard Mater 470 (2024) 134298.
[34] W. Peng, C. Liu, D. Chen, X. Duan, L. Zhong, Exposure to N-(1,3-dimethylbutyl)-N′-phenyl-p-phenylenediamine (6PPD) affects the growth and development of zebrafish embryos/larvae, Ecotoxicol. Environ. Saf. 232 (2022) 113221.
[35] J. Lam, D. Oh, L. Wong, D. Amarnani, C. Park-Windhol, A. Sanchez, J. Cardona-Velez, D. McGuone, A. Stemmer-Rachamimov, D. Eliott, D. Bielenberg, T. van Zyl, L. Shen, X. Gai, P. D'Amore, L. Kim, J. Arboleda-Velasquez, Identification of RUNX1 as a mediator of aberrant retinal angiogenesis, Diabetes 66 (7) (2017) 1950–1956.
[36] D. Li, X. Liu, T. Liu, H. Liu, L. Tong, S. Jia, Y.F. Wang, Neurochemical regulation of the expression and function of glial fibrillary acidic protein in astrocytes, Glia 68 (5) (2020) 878–897.
[37] A.M. Colangelo, L. Alberghina, M. Papa, Astrogliosis as a therapeutic target for neurodegenerative diseases, Neurosci. Lett. 565 (2014) 59–64.
[38] M. Kuzmanovic, V.J. Dudley, V.P. Sarthy, GFAP promoter drives müller cell-specific expression in transgenic mice, Investig. Ophthalmol. Vis. Sci. 44 (8) (2003) 3606–3613.
[39] I. Velzeboer, C.J.A.F. Kwadijk, A.A. Koelmans, Strong sorption of PCBs to nanoplastics, microplastics, carbon nanotubes, and fullerenes, Environ. Sci. Technol. 48 (9) (2014) 4869–4876.
[40] Q. Yuan, R. Sun, P. Yu, Y. Cheng, W. Wu, J. Bao, P. Alvarez, UV-aging of microplastics increases proximal ARG donor-recipient adsorption and leaching of chemicals that synergistically enhance antibiotic resistance propagation, J Hazard Mater (2021) 127895.
[41] G. Liu, Z. Zhu, Y. Yang, Y. Sun, F. Yu, J. Ma, Sorption behavior and mechanism of hydrophilic organic chemicals to virgin and aged microplastics in freshwater and seawater, Environ Pollut 246 (2019) 26–33.
[42] H. Zhang, J. Wang, B. Zhou, Y. Zhou, Z. Dai, Q. Zhou, P. Chriestie, Y. Luo, Enhanced adsorption of oxytetracycline to weathered microplastic polystyrene: kinetics, isotherms and influencing factors, Environ Pollut 243 (Pt B) (2018) 1550–1557.
[43] K. Wang, I. Vorontsova, M. Hoshino, K. Uesugi, N. Yagi, J.E. Hall, T.F. Schilling, B.K. Pierscionek, Optical development in the zebrafish eye lens, Faseb j 34 (4) (2020) 5552–5562.
[44] J. Chang, L. Zhang, J. Zhao, Z. Zhang, Z. Wang, H. Wang, B. Wan, 6PPD, not 6PPD-Quinone, induced serious zebrafish eye damage by disrupting the thyroid signaling pathway, Environ. Sci. Technol. 58 (50) (2024) 22076–22088.
[45] A. Cvekl, W.L. Wang, Retinoic acid signaling in Mammalian eye development, Exp. Eye Res. 89 (3) (2009) 280–291.
[46] R.K. Kam, Y. Deng, Y. Chen, H. Zhao, Retinoic acid synthesis and functions in

early embryonic development, Cell Biosci. 2 (1) (2012) 11.
[47] T. Sinha, L. Ikelle, M.I. Naash, M.R. Al-Ubaidi, The intersection of serine metabolism and cellular dysfunction in retinal degeneration, Cells 9 (3) (2020).
[48] Q. Chen, Y. Liu, L. Bi, L. Jin, R. Peng, Understanding the mechanistic roles of microplastics combined with heavy metals in regulating ferroptosis: adding new paradigms regarding the links with diseases, Environ. Res. 242 (2024) 117732.
[49] L. Yang, X. Cai, R. Li, Ferroptosis induced by pollutants: an emerging mechanism in environmental toxicology, Environ. Sci. Technol. 58 (5) (2024) 2166–2184.
[50] W. Hu, C. Zhou, Q. Jing, Y. Li, J. Yang, C. Yang, L. Wang, J. Hu, H. Li, H. Wang, C. Yuan, Y. Zhou, X. Ren, X. Tong, J. Du, Y. Wang, FTH promotes the proliferation and renders the HCC cells specifically resist to ferroptosis by maintaining iron homeostasis, Cancer Cell Int. 21 (1) (2021) 709.
[51] Y. Xuan, K. Peng, R. Zhu, Y. Kang, Z. Yin, Hmox1 is identified as a ferroptosis hub gene and associated with the M1 type microglia/macrophage polarization in spinal cord injury: bioinformatics and experimental validation, Mol. Neurobiol. 60 (12) (2023) 7151–7165.